JACS
JOURNAL OF THE AMERICAN CHEMICAL SOCIETY
pubs.acs.org/JACS
Article

Atomic Layers of B2 CuPd on Cu Nanocubes as Catalysts for Selective Hydrogenation

Qiang Gao,[#] Zihao Yan,[#] Weijie Zhang,[#] Hemanth Somarajan Pillai, Bingqing Yao, Wenjie Zang, Yuanqi Liu, Xue Han, Bokki Min, Hua Zhou, Lu Ma, Bukuru Anaclet, Sen Zhang, Hongliang Xin,* Qian He,* and Huiyuan Zhu*

Cite This: https://doi.org/10.1021/jacs.3c06514

ABSTRACT: The search for highly active and selective catalysts with high precious metal atom utilization efficiency has attracted increasing interest in both the fundamental synthesis of materials and important industrial reactions. Here, we report the synthesis of Pd−Cu nanocubes with a Cu core and an ordered B2 intermetallic CuPd shell with controllable atomic layers on the surface (denoted as Cu/B2 CuPd), which can efficiently and robustly catalyze the selective hydrogenation of acetylene (C_2H_2) to ethylene (C_2H_4) under mild conditions. The optimized Cu/B2 CuPd with a Pd loading of 9.5 at. % exhibited outstanding performance in the C_2H_2 semi-hydrogenation with 100% C_2H_2 conversion and 95.2% C_2H_4 selectivity at 90 °C. We attributed this outstanding performance to the core/shell structure with a high surface density of active Pd sites isolated by Cu in the B2 intermetallic matrix, representing a structural motif of single-atom alloys (SAAs) on the surface. The combined experimental and computational studies further revealed that the electronic states of Pd and Cu are modulated by SAAs from the synergistic effect between Pd and Cu, leading to enhanced performance compared with pristine Pd and Cu catalysts. This study provides a new synthetic methodology for making single-atom catalysts with high precious metal atom utilization efficiency, enabling simultaneous tuning of both geometric and electronic structures of Pd active sites for enhanced catalysis.

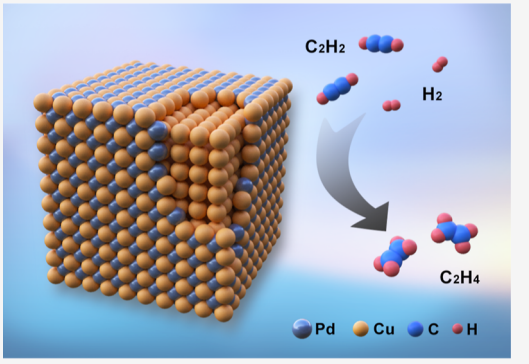

INTRODUCTION

Precious metal nanoparticles (NPs) like palladium (Pd) and platinum (Pt) play an essential role in many chemical catalytic reactions due to their unique chemical and physical properties.[1−4] Despite the merits, these precious metal NPs are not cost-effective nor optimized in selectivity toward desired products. For example, semi-hydrogenation of acetylene (C_2H_2) toward ethylene (C_2H_4) is an important industrial reaction because even a trace amount of C_2H_2 (∼1%) contained in the C_2H_4 stream from cracking of naphtha is poisonous to the downstream polymerization catalysts.[5−7] Consequently, C_2H_2 in the stream of C_2H_4 must be reduced to less than 5 ppm and an economic strategy is semi-hydrogenation of C_2H_2 to C_2H_4.[7,8] Pd NPs exhibit promising conversion of C_2H_2 in this reaction but suffer from limited selectivity, generating undesired ethane (C_2H_6) due to strong adsorption of C_2H_4 at contiguous Pd sites.[9,10] To date, three main strategies have been developed to improve the atom efficiency and the selectivity of Pd: (1) alloying Pd with a nonprecious 3d-transition metal, which however shifts down the d-band of Pd, leading to weakened adsorption of C_2H_4 to improve selectivity at a cost of conversion;[11−13] (2) constructing a porous metal-oxide coating on Pd to eliminate the formation of bulk Pd-hydrides;[14−16] and (3) diluting the continuous Pd ensembles till the limit of the single-atom regime to passivate some active sites for over-hydrogenation.[11,17,18] Among those three strategies, the single-atom catalysts (SACs) demonstrate the highest precious-metal atom utilization efficiency.[19−21] Nevertheless, it is still a challenge to develop highly active and selective catalysts with low loading but ultra-high surface density of isolated Pd atoms on the surface.

To date, the majority of SACs reported are single atoms anchored to a solid support (*e.g.*, metal oxides and carbon materials).[7,9] However, they suffer from a lack of control over the single-atom loading and potential aggregation under high-temperature reactive conditions.[10,22,23] Recently, a new system of single-atom alloys (SAAs) in which precious metal single atoms are embedded into a relatively inert host metal, has been reported.[24,25] Due to the metallic bonding between single atoms and the host metal, SAAs could exhibit higher stability

Received: June 20, 2023

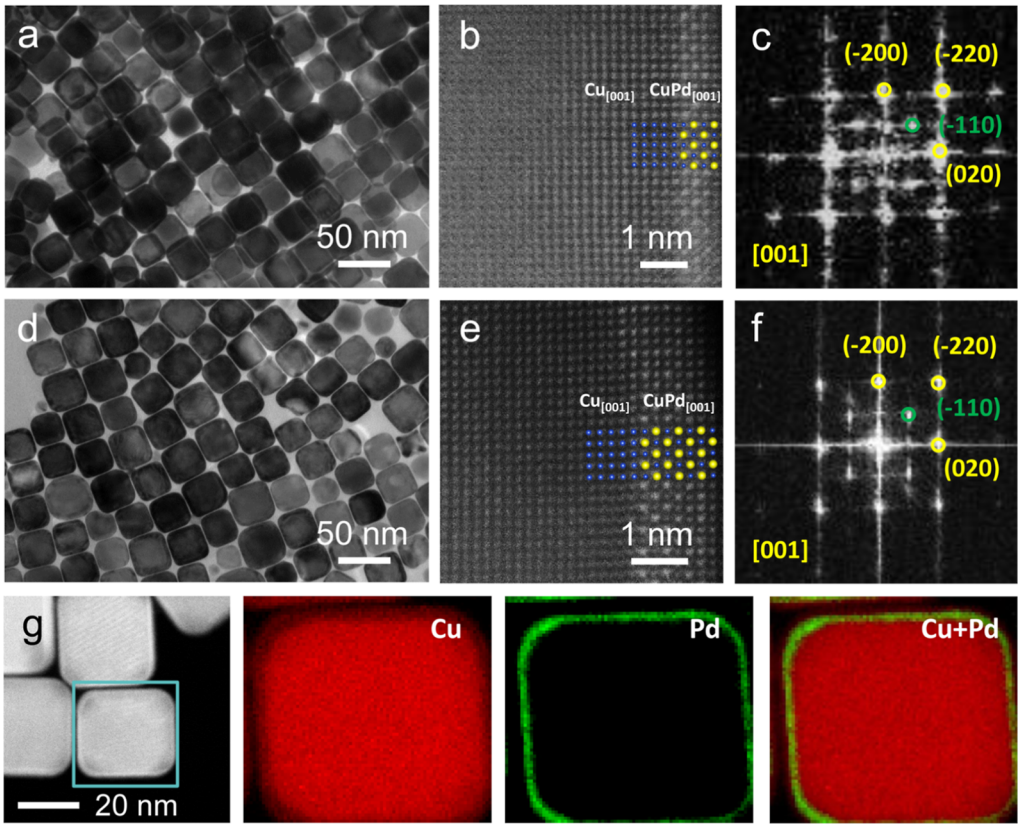

Figure 1. (a) TEM image of Cu/B2 CuPd-1 nanocubes. (b) Atomic-resolution HAADF-STEM image of a Cu/B2 CuPd-1 nanocube, and (c) corresponding FFT pattern of the CuPd shell. (d) TEM image of Cu/B2 CuPd-2 nanocubes. (e) Atomic-resolution HAADF-STEM image of a Cu/B2 CuPd-2 nanocube, and (f) corresponding FFT pattern of the CuPd shell. (g) STEM-EDX elemental mapping and the corresponding HAADF image of a Cu/B2 CuPd-2 nanocube.

than SACs anchored on supports.[26,27] More importantly, benefitting from the free-atom-like d-states, SAAs have been proved in theory to have the potential to break the linear scaling relations inherent to metal catalysts and improve the selectivity toward desired products.[28,29] Nevertheless, the synthesis of SAAs is mostly developed under ultrahigh-vacuum conditions[17,27,30] with only a few discrete examples of Pd-based SAA particle catalysts, *e.g.*, PdAg[31] and PdCu.[27,32] The development of well-defined, monodisperse SAA nanocrystals (NCs) is still in its infancy. We recently developed a strategy for controlled synthesis of Cu−Au SAA NCs with tunable single-site density.[33] Specifically, we employed an ordered intermetallic structure of tetragonal *P4/mmm* CuAu in which the Au atoms are isolated by the host metal Cu, representing a structural motif with the ultra-high density of single-atom sites.

Herein, we synthesized cubic core/shell NCs with a Cu core and an ordered intermetallic B2 CuPd shell (denoted as Cu/B2 CuPd) with controllable atomic layers (4 and 7 atomic layers). The ordered intermetallic layers of B2 CuPd can be considered as single-site Pd atoms isolated by 8 Cu atoms, representing the high density of single-atom Pd alloyed into a Cu matrix. With precious metal components present only in a few atomic layers on the surface and in the single-site state, this unique system inherits the merits of maximizing atom efficiency and selective stabilization of key reaction adsorbates. As a proof-of-concept, we further investigated the catalytic performance of Cu/B2 CuPd in the hydrogenation of C_2H_2 as a model reaction for more complex hydrogenation reactions. At 90 °C, the Cu/B2 CuPd with a relatively low Pd ratio (5.3 at. % Pd, denoted as Cu/B2 CuPd-1) exhibited 40% conversion of C_2H_2 and 99.2% C_2H_4 selectivity at 50 sccm of 0.5% C_2H_2 and 3% H_2 in Ar. In addition, the activity and selectivity can be tuned by adjusting the ratio of Pd in Cu/B2 CuPd. With a higher Pd ratio of 9.5 at. %, the Cu/B2 CuPd-2 readily achieved 100% C_2H_2 elimination with a 95.2% C_2H_4 selectivity under the same conditions. We found that increased Pd loading can significantly enhance the activity of Cu/B2 CuPd while still maintaining the C_2H_4 selectivity due to the isolated form of Pd sites in the B2 intermetallic CuPd shell.

RESULTS AND DISCUSSION

We used a seed-mediated approach to precisely deposit intermetallic CuPd on Cu nanocubes according to our modified previous method.[33] First, uniform Cu nanocubes with a size of 40 ± 3 nm were synthesized (Figure S1). A controlled amount of Pd precursor in oleylamine was injected dropwise into the solution, followed by 30 min of incubation (see details in the Supporting Information), to yield 4 and 7 atomic layers of B2 CuPd on Cu in Cu/B2 CuPd-1 and Cu/B2 CuPd-2, respectively. Transmission electron microscopy (TEM) image of the as-synthesized sample reveals uniform cubic morphology with a size of 43 ± 4 nm (Figure 1a). High-angle annular dark-field scanning TEM (HAADF-STEM) was used to characterize and analyze the fine structure of the Cu/B2 CuPd nanocubes. Atomic-resolution STEM image shows the distinct atomic contrast (*Z* contrast) where Pd (*Z* = 46) is brighter than Cu (*Z* = 29), which indicates that the nanocubes have a core/shell structure with epitaxial growth of an ordered

https://doi.org/10.1021/jacs.3c06514
J. Am. Chem. Soc. XXXX, XXX, XXX−XXX

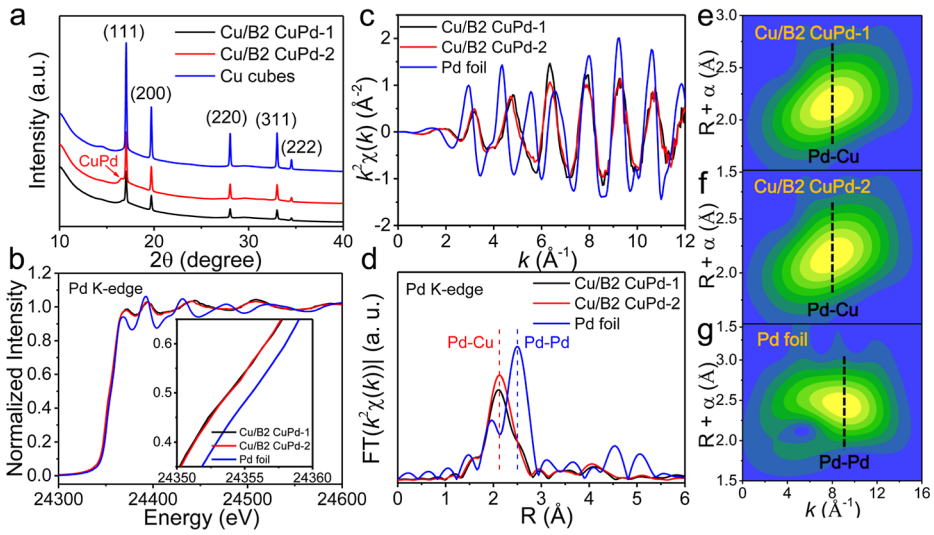

Figure 2. (a) Synchrotron XRD patterns of Cu/B2 CuPd nanocubes and Cu nanocubes. (b) Pd K-edge XANES spectra of Cu/B2 CuPd nanocubes and Pd foil reference, with a zoomed view of the Pd K-edge as inset. (c) EXAFS oscillation functions at the Pd K-edge of Cu/B2 CuPd nanocubes and Pd foil reference. (d) EXAFS Fourier transformed k2-weighted χ(k) function spectra of Cu/B2 CuPd nanocubes and Pd foil reference. (e–g) Pd K-edge WT EXAFS of Cu/B2 CuPd nanocubes and Pd foil reference.

intermetallic CuPd shell on the Cu core (Figure 1b). The atomic ordering in the CuPd nanocube can be directly visualized using *Z* contrast in the atomic-resolution HAADF-STEM images (Figures 1b and S2). As shown in Figure S2, the alternating intensity profile in the corresponding HAADF line profile further confirms the Pd/Cu atomic ordering within the CuPd shell. From the atomic-resolution HAADF-STEM image shown in Figure 1b, the number of ordered CuPd atomic layers is estimated to be 4. Moreover, the corresponding Fourier-transform (FFT) pattern of the CuPd shell depicted in Figure 1c shows bright dots that can be assigned to the (−110), (−200), (020), and (−220) planes of ordered CuPd B2 intermetallic phase, respectively.

The amount of Pd precursor plays a vital role in dictating the number of atomic layers in the intermetallic CuPd shell. As demonstrated in Figure 1d,e, Cu/B2 CuPd-2 nanocubes show a similar particle size to the Cu/B2 CuPd-1 nanocubes, while the number of ordered CuPd atomic layers is increased to 7 by adjusting the volume of the Pd precursor solution from 1 to 2 mL (see Supporting Information for details). The B2 intermetallic structure of CuPd shell can be directly observed from the atomic resolution HAADF-STEM image (Figures 1e and S3) and the corresponding FFT pattern of Figure 1e (Figure 1f). Elemental analysis was carried out to gain further insights into the distribution of Pd and Cu in the Cu/B2 CuPd-2 nanocubes. Figure 1g shows a HAADF-STEM image and the corresponding energy-dispersive X-ray spectroscopy (EDX) elemental mapping of a representative nanocube. While Pd and Cu are homogeneously distributed in the shell, only Cu is observed in the core, further confirming the core/shell structure of Cu/B2 CuPd.

Powder X-ray diffraction (XRD) patterns of Cu/B2 CuPd nanocubes demonstrate diffraction peaks that match well with Cu face-centered cubic (*fcc*) phase (Figure S4). Because the ordered intermetallic CuPd shell is only present in a few atomic layers, Panalytical's X-ray diffractometer could not detect the signal of the thin ordered intermetallic shell. Therefore, synchrotron XRD was performed to further characterize the crystal structure of the nanocubes. As shown in Figure 2a, in addition to those peaks detected in both Cu and Cu/B2 CuPd systems, a peak at 2θ = 16.4 was observed in the synchrotron XRD pattern of Cu/B2 CuPd-2, which can be assigned to the (110) peak of ordered B2 CuPd structure, consistent with our STEM results. The inductively coupled plasma optical emission spectrometry results suggested that the Pd atomic ratio is about 5.3 and 9.5 at. % for Cu/B2 CuPd-1 and Cu/B2 CuPd-2, which is equivalent to the Pd weight ratio of 8.5 and 15.0 wt %, respectively (Table S1).

The electronic interactions between Cu and Pd were investigated *via* X-ray absorption near-edge spectroscopy (XANES) of the Pd K-edge. The XANES spectra show that the absorption edge of the Pd K-edge for Cu/B2 CuPd shifts to the lower energy direction compared with Pd foil (Figure 2b), indicating the existence of charge transfer from Cu to Pd. The extended X-ray absorption fine structure (EXAFS) oscillations of Cu/B2 CuPd nanocubes are significantly different from that of Pd foil, with longer periods and smaller amplitudes (Figure 2c). The longer periods are due to the shorter Pd–Cu distances of Cu/B2 CuPd nanocubes than that of *fcc* phase Pd foil. Smaller amplitudes suggest the lower coordination number of Pd atoms in Cu/B2 CuPd nanocubes. As shown in Fourier-transformed Pd K-edge EXAFS spectra (Figure 2d), in comparison with Pd foil, the Cu/B2 CuPd nanocubes exhibit shorter interatomic distance $R_{Pd-Cu(Pd)}$ than that of cubic close-packed Pd, and the Pd–Pd bonds are absent in Cu/B2 CuPd nanocubes. In the *R* space, both Cu/B2 CuPd nanocubes exhibit a prominent peak at ∼2.12 Å from the Pd–Cu bonds, while no typical peaks for Pd–Pd bonds at higher *R* values can be found. EXAFS fitting was further conducted to obtain a quantitative structural configuration of Pd (Figures S5–S7 and Table S2). In comparison with Pd foil, both Cu/B2 CuPd nanocubes exhibit shorter interatomic distance $R_{Pd-Cu(Pd)}$ (∼2.57 Å) than that of *fcc* Pd foil (∼2.74 Å), and the Pd–Pd coordination is absent in Cu/B2 CuPd nanocubes. These results confirm that the Pd atoms in the CuPd are present in single atomic dispersion. The coordination number of Pd atoms in Cu/B2 CuPd-1 (5.99), Cu/B2 CuPd-2 nanocubes (7.8) is smaller than that in bulk Pd foil

https://doi.org/10.1021/jacs.3c06514
J. Am. Chem. Soc. XXXX, XXX, XXX–XXX

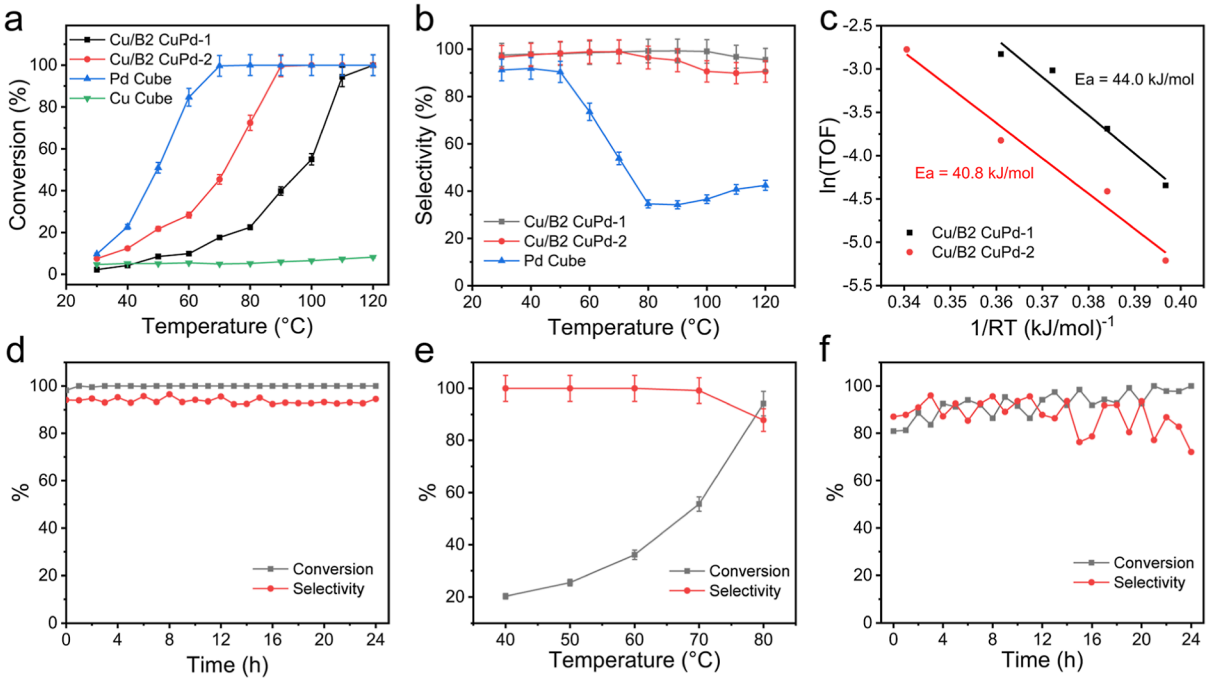

Figure 3. (a) C_2H_2 conversion and (b) C_2H_4 selectivity as a function of reaction temperature over the Cu/B2 CuPd-1, Cu/B2 CuPd-2, Cu nanocube, and Pd nanocube catalysts. Reaction conditions: 50 sccm of 0.5% C_2H_2 and 3% H_2 in Ar. Error bars represent the instrumental error (±5%). (c) Apparent activation energy of the Cu/B2 CuPd catalysts. (d) C_2H_2 conversion and C_2H_4 selectivity during the stability test at 90 °C for Cu/B2 CuPd-2. (e) Conversion and selectivity of Cu/B2 CuPd-2 as a function of reaction temperature under simulated front-end conditions (50 sccm of 0.5% C_2H_2, 5% H_2, and 10% of C_2H_4 balanced with Ar). (f) C_2H_2 conversion and C_2H_4 selectivity of Cu/B2 CuPd-2 during the stability test at 80 °C under the simulated front-end condition.

(12), consistent with the theoretical coordination number of 8 for ordered B2 CuPd intermetallic structure and 12 for Pd *fcc* structure. For the Cu K-edge, there is no apparent shift in the *R* space due to the presence of bulk Cu in the core (Figure S8). The wavelet transform (WT) of Pd K-edge EXAFS oscillations was performed and the corresponding contour plots of Cu/B2 CuPd nanocubes and Pd foil demonstrated intensity maxima at 8.5 $Å^{-1}$ of Pd foil which is associated with the Pd−Pd contribution (Figure 2g), while the WT contour plot of Cu/B2 CuPd nanocubes (Figure 2e,f) displays the maximum intensity at 8.1 $Å^{-1}$, which can be ascribed to the Pd−Cu bonding. Taken cumulatively, the above results suggest that the Pd sites are atomically dispersed in Cu/B2 CuPd systems.

With the unique surface intermetallic single-site structure, Cu/B2 CuPd nanocubes were loaded onto γ-Al_2O_3 (Figure S9) as catalysts for the semi-hydrogenation of C_2H_2 (see Supporting Information for details). The surfactants on the supported catalysts were removed by hydrazine treatment which was verified by Fourier transform infrared spectra (Figure S10).[34] As a comparison, ∼40 nm Cu nanocubes (Figure S1) and ∼12 nm Pd nanocubes (Figure S11) were synthesized and tested. A gas mixture containing 0.5% C_2H_2 and 3% H_2 balanced with Ar was fed into the reactor at 50 sccm, corresponding to a space velocity of 15,000 mL h^{-1} g^{-1}. Figure 3a,b summarizes the C_2H_2 conversion and C_2H_4 selectivity against the reaction temperature. At 90 °C, Cu/B2 CuPd-2 exhibited a 100% C_2H_2 conversion and 95.2% C_2H_4 selectivity while the Cu/B2 CuPd-1 exhibited a 40% conversion and 99.2% C_2H_4 selectivity. The apparent activation energy (Ea) of Cu/B2 CuPd-1 and Cu/B2 CuPd-2 was 44.0 and 40.8 kJ/mol, respectively (Figure 3c) which are close to literature values of Pd-based SAAs.[31,32] Note that the amount of Cu/B2 CuPd-2 was controlled to ensure the conversions within the true kinetics regime (<10%) for an accurate Ea calculation. The close Ea values agree with our expectation that Cu/B2 CuPd-1 and Cu/B2 CuPd-1 exhibit identical surface structures of B2 CuPd and thus intrinsic activities. The TOF values (s^{-1}) were calculated to be 0.24 and 0.69 for Cu/B2 CuPd-1 and Cu/B2 CuPd-2 respectively at 90 °C. We noticed that the selectivity of Cu/B2 CuPd-2 slightly dropped after we raised the temperature above 90 °C. This is because the excess heating did not favor the exothermal reaction (ΔH_0 = −176 kJ/mol) and the reactant C_2H_2 was exhausted before leaving the catalyst bed.[35] Nevertheless, the selectivity of the Cu/B2 CuPd-2 still maintains a high selectivity (>90%), indicating an operation window of at least 30° (90 to 120 °C). Under the same reaction conditions, the Pd nanocubes exhibited 100% C_2H_2 conversion at 70 °C with a 51% C_2H_4 selectivity while the Cu nanocube exhibited negligible conversion up to 120 °C (Figure 3a). CuPd alloy nanoparticles with an *fcc* structure were also synthesized as a comparison (Figure S12).[36] As shown in Figure S13, the CuPd random alloy nanoparticles exhibited high selectivity at low temperatures. However, when the conversion approached 100% at 60 °C, the selectivity dropped abruptly to 75%, implying a very small operation window. The dissimilar catalytic behaviors between the CuPd random alloy nanoparticles and Cu/B2 CuPd nanocubes suggest the promoting effect of single-atom sites in addition to the alloying effect with Cu.

The stability test was carried out for Cu/B2 CuPd-2 at both high and low C_2H_2 conversions. As illustrated in Figures 3d and S14, the Cu/B2 CuPd nanocubes showed no apparent decrease in conversion and selectivity under both conditions

https://doi.org/10.1021/jacs.3c06514
J. Am. Chem. Soc. XXXX, XXX, XXX−XXX

during the 24h stability measurements. Specifically, at 90 °C, the average C_2H_2 conversion was 99.9% (standard deviation, STD = 0.36%) and the average C_2H_4 selectivity was 93.7% (STD = 1.18%), which are close to the values of 100 and 95.2% respectively in the activity test. In addition, TEM and HAADF-STEM images demonstrate that the Cu/B2 CuPd-2 exhibited well-maintained morphology and structure after the stability test (Figure S15).

Industrially, compared with tail-end configurations where a stoichiometric amount of H_2 is fed, the front-end condition with excess H_2 and C_2H_4 poses greater challenges due to more favorable over-hydrogenation toward C_2H_6.[31,32] To simulate front-end conditions, we fed gas mixtures with a $C_2H_2/H_2/C_2H_4$ ratio of 1:10:20 balanced with Ar. As illustrated in Figure 3e, Cu/B2 CuPd-2 achieved 94.2% C_2H_2 conversion and 87.8% C_2H_4 selectivity at 80 °C under the simulated front-end condition. During a 24 h stability test, Cu/B2 CuPd-2 exhibited an average C_2H_2 conversion of 92.5% (STD = 5.5%) with an average C_2H_4 selectivity of 87.7% (STD = 6.6%) (Figure 3f).

In situ diffuse reflectance infrared Fourier transform spectroscopy (DRIFTS) experiments on CO adsorption were conducted to explore the geometric and electronic structures of Cu/B2 CuPd-1, Cu/B2 CuPd-2, Pd nanocubes, and Cu nanocubes (Figures 4 and S16–S18). The linear CO

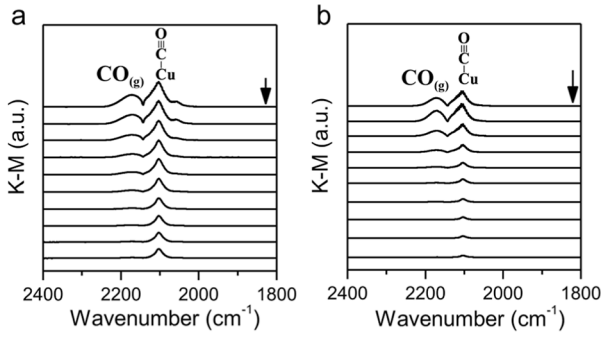

Figure 4. *In situ* DRIFTS spectra of CO adsorption on the Cu/B2 CuPd-1 (a) and Cu/B2 CuPd-2 (b) catalysts.

vibrational frequency on Cu/B2 CuPd-1 and Cu/B2 CuPd-2 was 2107 cm^{-1}, close to that of Cu nanocubes (Figure S16b). Moreover, the bridge adsorption of CO at 1951 cm^{-1} on Pd cubes was not observed on Cu/B2 CuPd-1 and Cu/B2 CuPd-2 (Figure S17). These results indicated that the Pd atoms are isolated in a Cu lattice, which leads to high C_2H_4 selectivity as we observed in catalytic studies. To investigate the evolution of surface-adsorbed CO, the DRIFTS study of CO sorption was performed by collecting spectra at different times (Figure S18). The decreasing characteristic bands of Cu/B2 CuPd-1 and Cu/B2 CuPd-2 at 2107 cm^{-1} could be found in the time-resolved DRIFTS spectra in the atmosphere of N_2 flow (Figure S19). Given that Cu/B2 CuPd-1 has a lower rate of decrease in peak intensity, we attribute these to its predominant charge transfer from Cu to Pd atoms in the $Pd^{\delta-}$-$Cu^{\delta+}$ atom pairs.[37]

Density functional theory (DFT) calculations at the PBE + D3 level were performed in order to better understand the performance of the Cu/B2 CuPd nanocubes when compared to Pd nanocubes. Model systems were generated using the (110) terrace for the B2 CuPd structure (as determined in Figures 1 and S2, S3) and the (100) terrace for the Pd nanocubes. Figure 5 plots the formation free energies for

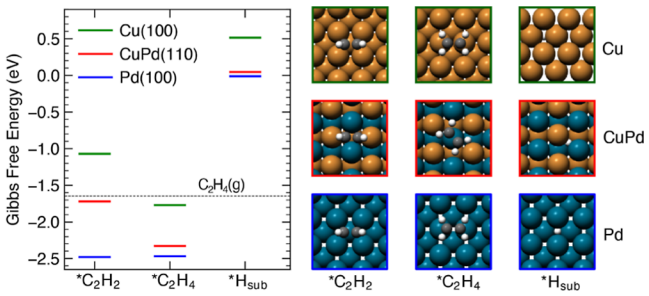

Figure 5. Standard free formation energies at 298.15 K for $*C_2H_2$, $*C_2H_4$, and $*H_{sub}$ on Cu(100), CuPd(110), and Pd(100) surfaces. The horizontal black line indicates the $C_2H_4(g)$ formation free energy. Formation free energies are calculated based on the clean surface, $C_2H_2(g)$, and $H_2(g)$ as the references. Structures are shown where white represents hydrogen, grey represents carbon, brown represents copper, and blue represents palladium.

$*C_2H_2$, $*C_2H_4$, and a subsurface *H with geometries shown below. It can be seen that Pd binds $*C_2H_2$ strongest with a formation free energy of −2.50 eV, allowing for easy activation at low temperatures. However, concomitantly the stronger $*C_2H_4$ binding leads to further hydrogenation which hampers its selectivity. On the other hand, the B2 CuPd structure binds $*C_2H_2$ and $*C_2H_4$ weaker by 0.8 and 0.2 eV, respectively, thus requiring a higher temperature to achieve 100% conversion. *In situ* DRIFTS experiments on C_2H_2 adsorption were performed to figure out the conformations of C_2H_2 species on the surface (Figure S20). The bands at 2978 cm^{-1} can be assigned to the di-σ-bonded C_2H_2 species on the surface of Pd cubes (Figure S20c).[38] DFT-computed C−H stretch frequencies on Pd(100) are 2984 and 2962 cm^{-1} for the symmetric and asymmetric modes, respectively (Table S3). The adsorption of C_2H_2 species on Cu/B2 CuPd was obviously weaker than Pd cubes, consistent with our DFT calculations. Regarding the adsorption of C_2H_4, from the geometry analysis, the Pd surface prefers di-σ-bonding of the $*C_2H_4$ due to the contiguous Pd sites while the single-site nature of Pd sites in the B2 CuPd structure leads to the formation of π-bonding $*C_2H_4$. This difference in adsorption modes leads to a weaker binding and thus easier desorption of the C_2H_4.[26,27,32] A slightly compressive strain of the (110)-oriented surface CuPd layers imposed by the Cu core, although expected to be mostly relaxed beyond 4 layers, will further weaken its adsorption. As shown in Figure S21, the peaks around 1445 cm^{-1} can be assigned to di-σ-bonded C_2H_4 for four samples, similar to DFT-computed values of the C=C stretch model on Cu(100) and Pd(100) surfaces (Table S4).[12] Chemisorbed species adsorbed on Pd cubes after purging N_2 for 60 min are both di-σ-bonded and π-bonded C_2H_4 species (Figure S22). However, the C_2H_4 is mainly adsorbed on Cu/B2 CuPd-2 in π-bonding mode (peaks around 1630 cm^{-1}).[39] In addition to the weaker binding of key intermediates, the B2 CuPd structure also has a weaker formation energy for the subsurface hydrogen of 0.1 eV when compared to Pd. This is important in preventing the formation of subsurface hydrides which can take part in the further hydrogenation of $*C_2H_4$ to unwanted products.[16,40] Another factor to be considered is the electronic structure of the Pd single atom site. Since Pd has larger electronegativity than Cu, electrons tend to transfer from Cu to Pd, making Pd single atoms negatively charged in accordance with our XANES results (Figure 2b), which tends to "repel" the C_2H_4

https://doi.org/10.1021/jacs.3c06514
J. Am. Chem. Soc. XXXX, XXX, XXX−XXX

molecule, lowering its adsorption energy, and enhance the selectivity.

CONCLUSIONS

In summary, we present here a novel, facile, and controllable method for synthesizing SAA Cu/B2 CuPd nanocubes with a Cu core and an ordered B2 intermetallic CuPd shell, which can efficiently and robustly catalyze selectively hydrogenation of C_2H_2 to C_2H_4 at mild conditions. The Cu/B2 CuPd SAA nanocubes exhibited outstanding performance in the C_2H_2 semi-hydrogenation, with 100% C_2H_2 conversion and 95.2% C_2H_4 selectivity at 90 °C. The combined experimental/computational study sheds crucial light on understanding the observation of remarkable stability and outstanding performance. Such a structural motif of SAAs on the surfaces not only stabilizes the isolated precious metals with high surface density to avoid segregation but also generates a charge transfer within Cu−Pd atom pairs to enhance the catalytic performance. This new method achieved simultaneous tuning of both the geometric and electronic structure of the Pd active sites which resulted in highly active and stable catalysts.

ASSOCIATED CONTENT

Supporting Information

The Supporting Information is available free of charge at https://pubs.acs.org/doi/10.1021/jacs.3c06514.

Experimental details, supporting figures with additional data, and detailed information on DFT calculation (PDF)

AUTHOR INFORMATION

Corresponding Authors

Hongliang Xin − *Department of Chemical Engineering, Virginia Polytechnic Institute and State University, Blacksburg, Virginia 24061, United States;* orcid.org/0000-0001-9344-1697; Email: hxin@vt.edu

Qian He − *Department of Materials Science and Engineering, National University of Singapore, Singapore 117575, Singapore*; Email: heqian@nus.edu.sg

Huiyuan Zhu − *Department of Chemistry, University of Virginia, Charlottesville, Virginia 22904, United States;* orcid.org/0000-0002-9962-1661; Email: kkx8js@virginia.edu

Authors

Qiang Gao − *Department of Chemistry, University of Virginia, Charlottesville, Virginia 22904, United States*

Zihao Yan − *Department of Chemistry, University of Virginia, Charlottesville, Virginia 22904, United States;* orcid.org/0000-0002-2640-1254

Weijie Zhang − *Department of Chemistry, University of Virginia, Charlottesville, Virginia 22904, United States*

Hemanth Somarajan Pillai − *Department of Chemical Engineering, Virginia Polytechnic Institute and State University, Blacksburg, Virginia 24061, United States;* orcid.org/0000-0003-3131-7396

Bingqing Yao − *Department of Materials Science and Engineering, National University of Singapore, Singapore 117575, Singapore*

Wenjie Zang − *Department of Materials Science and Engineering, National University of Singapore, Singapore 117575, Singapore*

Yuanqi Liu − *Department of Chemistry, University of Virginia, Charlottesville, Virginia 22904, United States*

Xue Han − *Department of Chemical Engineering, Virginia Polytechnic Institute and State University, Blacksburg, Virginia 24061, United States*

Bokki Min − *Department of Chemistry, University of Virginia, Charlottesville, Virginia 22904, United States*

Hua Zhou − *X-ray Science Division, Advanced Photon Source, Argonne National Laboratory, Lemont, Illinois 60439, United States;* orcid.org/0000-0001-9642-8674

Lu Ma − *National Synchrotron Light Source II (NSLS-II), Brookhaven National Laboratory, Upton, New York 11973, United States*

Bukuru Anaclet − *Department of Chemistry, University of Virginia, Charlottesville, Virginia 22904, United States*

Sen Zhang − *Department of Chemistry, University of Virginia, Charlottesville, Virginia 22904, United States;* orcid.org/0000-0002-1716-3741

Complete contact information is available at: https://pubs.acs.org/10.1021/jacs.3c06514

Author Contributions

#Q.G., Z.Y., and W.Z. authors contributed equally to this work.

Notes

The authors declare no competing financial interest.

ACKNOWLEDGMENTS

We acknowledge the funding support from NSF CBET Catalysis (Award # 2317302). Part of this work is also supported by the ACS Petroleum Research Foundation. S.Z., W.Z., and B.A. acknowledge the support from the Sloan Research Fellowship. H.S.P. and H.X. acknowledge the financial support from the NSF CAREER program (CBET-1845531). The computational resource used in this work is provided by the advanced research computing at Virginia Polytechnic Institute and State University. Q.H. would like to acknowledge the support by the National Research Foundation (NRF) Singapore, under its NRF Fellowship (NRF-NRFF11-2019-0002), the support from Singapore Low-carbon energy research funding initiative (Award ID LCERFI01-0017). This research used resources of the Advanced Photon Source, a U.S. Department of Energy (DOE) Office of Science user facility operated for the DOE Office of Science by Argonne National Laboratory under Contract no. DE-AC02-06CH11357. This research used 7-BM of the National Synchrotron Light Source II, a U.S. Department of Energy (DOE) Office of Science User Facility operated for the DOE Office of Science by Brookhaven National Laboratory under Contract no. DE-SC0012704.

REFERENCES

(1) Dann, E. K.; Gibson, E. K.; Blackmore, R. H.; Catlow, C. R. A.; Collier, P.; Chutia, A.; Erden, T. E.; Hardacre, C.; Kroner, A.; Nachtegaal, M.; Raj, A.; Rogers, S. M.; Taylor, S. F. R.; Thompson, P.; Tierney, G. F.; Zeinalipour-Yazdi, C. D.; Goguet, A.; Wells, P. P. Structural selectivity of supported Pd nanoparticles for catalytic NH_3 oxidation resolved using combined operando spectroscopy. *Nat. Catal.* **2019**, *2*, 157−163.

(2) Liu, P.; Zhao, Y.; Qin, R.; Mo, S.; Chen, G.; Gu, L.; Chevrier, D. M.; Zhang, P.; Guo, Q.; Zang, D.; Wu, B.; Fu, G.; Zheng, N. Photochemical route for synthesizing atomically dispersed palladium catalysts. *Science* **2016**, *352*, 797−800.

(3) Chen, G.; Xu, C.; Huang, X.; Ye, J.; Gu, L.; Li, G.; Tang, Z.; Wu, B.; Yang, H.; Zhao, Z.; Zhou, Z.; Fu, G.; Zheng, N. Interfacial

electronic effects control the reaction selectivity of platinum catalysts. *Nat. Mater.* **2016**, *15*, 564−569.
(4) Cargnello, M.; Doan-Nguyen, V. V. T.; Gordon, T. R.; Diaz, R. E.; Stach, E. A.; Gorte, R. J.; Fornasiero, P.; Murray, C. B. Control of Metal Nanocrystal Size Reveals Metal-Support Interface Role for Ceria Catalysts. *Science* **2013**, *341*, 771−773.
(5) Zhang, L.; Zhou, M.; Wang, A.; Zhang, T. Selective Hydrogenation over Supported Metal Catalysts: From Nanoparticles to Single Atoms. *Chem. Rev.* **2020**, *120*, 683−733.
(6) Turner, J. A. Sustainable Hydrogen Production. *Science* **2004**, *305*, 972−974.
(7) McCue, A. J.; Anderson, J. A. Recent advances in selective acetylene hydrogenation using palladium containing catalysts. *Front. Chem. Sci. Eng.* **2015**, *9*, 142−153.
(8) Bos, A. N. R.; Westerterp, K. R. Mechanism and kinetics of the selective hydrogenation of ethyne and ethene. *Chem. Eng. Process.: Process Intensif.* **1993**, *32*, 1−7.
(9) Teschner, D.; Borsodi, J.; Wootsch, A.; Révay, Z.; Hävecker, M.; Knop-Gericke, A.; Jackson, S. D.; Schlögl, R. The Roles of Subsurface Carbon and Hydrogen in Palladium-Catalyzed Alkyne Hydrogenation. *Science* **2008**, *320*, 86−89.
(10) Studt, F.; Abild-Pedersen, F.; Bligaard, T.; Sørensen, R. Z.; Christensen, C. H.; Nørskov, J. K. Identification of Non-Precious Metal Alloy Catalysts for Selective Hydrogenation of Acetylene. *Science* **2008**, *320*, 1320−1322.
(11) Hu, M.; Zhang, J.; Zhu, W.; Chen, Z.; Gao, X.; Du, X.; Wan, J.; Zhou, K.; Chen, C.; Li, Y. 50 ppm of Pd dispersed on $Ni(OH)_2$ nanosheets catalyzing semi-hydrogenation of acetylene with high activity and selectivity. *Nano Res.* **2018**, *11*, 905−912.
(12) Cao, Y.; Sui, Z.; Zhu, Y.; Zhou, X.; Chen, D. Selective Hydrogenation of Acetylene over Pd-In/Al_2O_3 Catalyst: Promotional Effect of Indium and Composition-Dependent Performance. *ACS Catal.* **2017**, *7*, 7835−7846.
(13) Kim, S. K.; Lee, J. H.; Ahn, I. Y.; Kim, W.-J.; Moon, S. H. Performance of Cu-promoted Pd catalysts prepared by adding Cu using a surface redox method in acetylene hydrogenation. *Appl. Catal. A: Gen.* **2011**, *401*, 12−19.
(14) Yan, Z.; Yao, B.; Hall, C.; Gao, Q.; Zang, W.; Zhou, H.; He, Q.; Zhu, H. Metal−Metal Oxide Catalytic Interface Formation and Structural Evolution: A Discovery of Strong Metal−Support Bonding, Ordered Intermetallics, and Single Atoms. *Nano Lett.* **2022**, *22*, 8122−8129.
(15) Liu, K.; Jiang, L.; Huang, W.; Zhu, G.; Zhang, Y.-J.; Xu, C.; Qin, R.; Liu, P.; Hu, C.; Wang, J.; Li, J.-F.; Yang, F.; Fu, G.; Zheng, N. Atomic overlayer of permeable microporous cuprous oxide on palladium promotes hydrogenation catalysis. *Nat. Commun.* **2022**, *13*, 2597.
(16) Wu, P.; Tan, S.; Moon, J.; Yan, Z.; Fung, V.; Li, N.; Yang, S.-Z.; Cheng, Y.; Abney, C. W.; Wu, Z.; Savara, A.; Momen, A. M.; Jiang, D.-e.; Su, D.; Li, H.; Zhu, W.; Dai, S.; Zhu, H. Harnessing strong metal−support interactions via a reverse route. *Nat. Commun.* **2020**, *11*, 3042.
(17) Kruppe, C. M.; Krooswyk, J. D.; Trenary, M. Selective Hydrogenation of Acetylene to Ethylene in the Presence of a Carbonaceous Surface Layer on a Pd/Cu(111) Single-Atom Alloy. *ACS Catal.* **2017**, *7*, 8042−8049.
(18) Huang, X.; Xia, Y.; Cao, Y.; Zheng, X.; Pan, H.; Zhu, J.; Ma, C.; Wang, H.; Li, J.; You, R.; Wei, S.; Huang, W.; Lu, J. Enhancing both selectivity and coking-resistance of a single-atom Pd1/C_3N_4 catalyst for acetylene hydrogenation. *Nano Res.* **2017**, *10*, 1302−1312.
(19) Wang, A.; Li, J.; Zhang, T. Heterogeneous single-atom catalysis. *Nat. Rev. Chem* **2018**, *2*, 65−81.
(20) Yang, X.-F.; Wang, A.; Qiao, B.; Li, J.; Liu, J.; Zhang, T. Single-Atom Catalysts: A New Frontier in Heterogeneous Catalysis. *Acc. Chem. Res.* **2013**, *46*, 1740−1748.
(21) Qiao, B.; Wang, A.; Yang, X.; Allard, L. F.; Jiang, Z.; Cui, Y.; Liu, J.; Li, J.; Zhang, T. Single-atom catalysis of CO oxidation using Pt1/FeO_x. *Nat. Chem.* **2011**, *3*, 634−641.
(22) Sun, M.; Ji, J.; Hu, M.; Weng, M.; Zhang, Y.; Yu, H.; Tang, J.; Zheng, J.; Jiang, Z.; Pan, F.; Liang, C.; Lin, Z. Overwhelming the Performance of Single Atoms with Atomic Clusters for Platinum-Catalyzed Hydrogen Evolution. *ACS Catal.* **2019**, *9*, 8213−8223.
(23) Kunwar, D.; Zhou, S.; DeLaRiva, A.; Peterson, E. J.; Xiong, H.; Pereira-Hernández, X. I.; Purdy, S. C.; ter Veen, R.; Brongersma, H. H.; Miller, J. T.; Hashiguchi, H.; Kovarik, L.; Lin, S.; Guo, H.; Wang, Y.; Datye, A. K. Stabilizing High Metal Loadings of Thermally Stable Platinum Single Atoms on an Industrial Catalyst Support. *ACS Catal.* **2019**, *9*, 3978−3990.
(24) Shen, T.; Wang, S.; Zhao, T.; Hu, Y.; Wang, D. Recent Advances of Single-Atom-Alloy for Energy Electrocatalysis. *Adv. Energy Mater.* **2022**, *12*, 2201823.
(25) Hannagan, R. T.; Giannakakis, G.; Flytzani-Stephanopoulos, M.; Sykes, E. C. H. Single-Atom Alloy Catalysis. *Chem. Rev.* **2020**, *120*, 12044−12088.
(26) Feng, Q.; Zhao, S.; Wang, Y.; Dong, J.; Chen, W.; He, D.; Wang, D.; Yang, J.; Zhu, Y.; Zhu, H.; Gu, L.; Li, Z.; Liu, Y.; Yu, R.; Li, J.; Li, Y. Isolated Single-Atom Pd Sites in Intermetallic Nanostructures: High Catalytic Selectivity for Semihydrogenation of Alkynes. *J. Am. Chem. Soc.* **2017**, *139*, 7294−7301.
(27) Kyriakou, G.; Boucher, M. B.; Jewell, A. D.; Lewis, E. A.; Lawton, T. J.; Baber, A. E.; Tierney, H. L.; Flytzani-Stephanopoulos, M.; Sykes, E. C. H. Isolated Metal Atom Geometries as a Strategy for Selective Heterogeneous Hydrogenations. *Science* **2012**, *335*, 1209−1212.
(28) Spivey, T. D.; Holewinski, A. Selective Interactions between Free-Atom-like d-States in Single-Atom Alloy Catalysts and Near-Frontier Molecular Orbitals. *J. Am. Chem. Soc.* **2021**, *143*, 11897−11902.
(29) Greiner, M. T.; Jones, T. E.; Beeg, S.; Zwiener, L.; Scherzer, M.; Girgsdies, F.; Piccinin, S.; Armbrüster, M.; Knop-Gericke, A.; Schlögl, R. Free-atom-like d states in single-atom alloy catalysts. *Nat. Chem.* **2018**, *10*, 1008−1015.
(30) Lucci, F. R.; Liu, J.; Marcinkowski, M. D.; Yang, M.; Allard, L. F.; Flytzani-Stephanopoulos, M.; Sykes, E. C. H. Selective hydrogenation of 1,3-butadiene on platinum−copper alloys at the single-atom limit. *Nat. Commun.* **2015**, *6*, 8550.
(31) Pei, G. X.; Liu, X. Y.; Wang, A.; Lee, A. F.; Isaacs, M. A.; Li, L.; Pan, X.; Yang, X.; Wang, X.; Tai, Z.; Wilson, K.; Zhang, T. Ag Alloyed Pd Single-Atom Catalysts for Efficient Selective Hydrogenation of Acetylene to Ethylene in Excess Ethylene. *ACS Catal.* **2015**, *5*, 3717−3725.
(32) Pei, G. X.; Liu, X. Y.; Yang, X.; Zhang, L.; Wang, A.; Li, L.; Wang, H.; Wang, X.; Zhang, T. Performance of Cu-Alloyed Pd Single-Atom Catalyst for Semihydrogenation of Acetylene under Simulated Front-End Conditions. *ACS Catal.* **2017**, *7*, 1491−1500.
(33) Gao, Q.; Yao, B.; Pillai, H. S.; Zang, W.; Han, X.; Liu, Y.; Yu, S.-W.; Yan, Z.; Min, B.; Zhang, S.; Zhou, H.; Ma, L.; Xin, H.; He, Q.; Zhu, H. Synthesis of core/shell nanocrystals with ordered intermetallic single-atom alloy layers for nitrate electroreduction to ammonia. *Nat. Synth.* **2023**, *2*, 624−634.
(34) Zhang, Z.; Chi, M.; Veith, G. M.; Zhang, P.; Lutterman, D. A.; Rosenthal, J.; Overbury, S. H.; Dai, S.; Zhu, H. Rational Design of Bi Nanoparticles for Efficient Electrochemical CO_2 Reduction: The Elucidation of Size and Surface Condition Effects. *ACS Catal.* **2016**, *6*, 6255−6264.
(35) Kuo, C.-T.; Lu, Y.; Kovarik, L.; Engelhard, M.; Karim, A. M. Structure Sensitivity of Acetylene Semi-Hydrogenation on Pt Single Atoms and Subnanometer Clusters. *ACS Catal.* **2019**, *9*, 11030−11041.
(36) Gao, Q.; Ju, Y. M.; An, D.; Gao, M. R.; Cui, C. H.; Liu, J. W.; Cong, H. P.; Yu, S. H. Shape-controlled synthesis of monodisperse PdCu nanocubes and their electrocatalytic properties. *ChemSusChem* **2013**, *6*, 1878−1882.
(37) Zhang, Z.; Chen, S.; Zhu, J.; Ye, C.; Mao, Y.; Wang, B.; Zhou, G.; Mai, L.; Wang, Z.; Liu, X.; Wang, D. Charge-Separated $Pd^{\delta-}$−$Cu^{\delta+}$ Atom Pairs Promote CO_2 Reduction to C2. *Nano Lett.* **2023**, *23*, 2312−2320.

https://doi.org/10.1021/jacs.3c06514
J. Am. Chem. Soc. XXXX, XXX, XXX−XXX

(38) Cao, T.; You, R.; Zhang, X.; Chen, S.; Li, D.; Zhang, Z.; Huang, W. An in situ DRIFTS mechanistic study of CeO_2-catalyzed acetylene semihydrogenation reaction. *Phys. Chem. Chem. Phys.* **2018**, *20*, 9659−9670.
(39) Li, B.; Zhang, Y.; Krishna, R.; Yao, K.; Han, Y.; Wu, Z.; Ma, D.; Shi, Z.; Pham, T.; Space, B.; Liu, J.; Thallapally, P. K.; Liu, J.; Chrzanowski, M.; Ma, S. Introduction of π-Complexation into Porous Aromatic Framework for Highly Selective Adsorption of Ethylene over Ethane. *J. Am. Chem. Soc.* **2014**, *136*, 8654−8660.
(40) Aleksandrov, H. A.; Kozlov, S. M.; Schauermann, S.; Vayssilov, G. N.; Neyman, K. M. How Absorbed Hydrogen Affects the Catalytic Activity of Transition Metals. *Angew. Chem., Int. Ed.* **2014**, *53*, 13371−13375.

https://doi.org/10.1021/jacs.3c06514
J. Am. Chem. Soc. XXXX, XXX, XXX−XXX